CHANDRA AND *SUZAKU* OBSERVATIONS OF THE Be/X-RAY STAR HD110432

J. M. Torrejón[1], N. S. Schulz[2], AND M. A. Nowak[2]

[1] Instituto de Física Aplicada a las Ciencias y las Tecnologías, Universidad de Alicante, E03080 Alicante, Spain; jmt@ua.es
[2] MIT Kavli Institute for Astrophysics and Space Research, Cambridge, MA 02139, USA

ABSTRACT

We present an analysis of a pointed 141 ks *Chandra* high-resolution transmission gratings observation of the Be X-ray emitting star HD110432, a prominent member of the γ Cas analogs. This observation represents the first high-resolution spectrum taken for this source as well as the longest uninterrupted observation of any γ Cas analog. The *Chandra* light curve shows a high variability but its analysis fails to detect any coherent periodicity up to a frequency of 0.05 Hz. Hardness ratio versus intensity analyses demonstrate that the relative contributions of the [1.5–3] Å, [3–6] Å, and [6–16] Å energy bands to the total flux change rapidly in the short term. The analysis of the *Chandra* High Energy Transmission Grating (HETG) spectrum shows that, to correctly describe the spectrum, three model components are needed. Two of those components are optically thin thermal plasmas of different temperatures ($kT \approx 8$–9 and 0.2–0.3 keV, respectively) described by the models `vmekal` or `bvapec`. The Fe abundance in each of these two components appears equal within the errors and is slightly subsolar with $Z \approx 0.75 \, Z_\odot$. The `bvapec` model better describes the Fe L transitions, although it cannot fit well the Na XI Lyα line at 10.02 Å, which appears to be overabundant. Two different models seem to describe well the third component. One possibility is a third hot optically thin thermal plasma at $kT = 16$–21 keV with an Fe abundance $Z \approx 0.3 \, Z_\odot$, definitely smaller than for the other two thermal components. Furthermore, the `bvapec` model describes well the Fe K shell transitions because it accounts for the turbulence broadening of the Fe XXV and Fe XXVI lines with a $v_{\text{turb}} \approx 1200 \, \text{km s}^{-1}$. These two lines, contributed mainly by the hot thermal plasma, are significantly wider than the Fe Kα line whose FWHM < 5 mÅ is not resolved by *Chandra*. Alternatively, the third component can be described by a power law with a photon index of $\Gamma = 1.56$. In either case, the *Chandra* HETG spectrum establishes that each one of these components must be modified by distinct absorption columns. The analysis of a noncontemporaneous 25 ks *Suzaku* observation shows the presence of a hard tail extending up to at least 33 keV. The *Suzaku* spectrum is described with the sum of two components: an optically thin thermal plasma at $kT \approx 9$ keV and $Z \approx 0.74 \, Z_\odot$, and a very hot second plasma with $kT \approx 33$ keV or, alternatively, a power law with photon index of $\Gamma = 1.58$. In either case, each one of the two components must be affected by different absorption columns. Therefore, the $kT = 8$–9 keV component is definitely needed while the nature of the harder emission cannot be unambiguously established with the present data sets. The analysis of the Si XIII and S XV He-like triplets present in the *Chandra* spectrum points to a very dense ($n_e \sim 10^{13} \, \text{cm}^{-3}$) plasma located either close to the stellar surface ($r < 3R_*$) of the Be star or, alternatively, very close ($r \sim 1.5R_{\text{WD}}$) to the surface of a (hypothetical) white dwarf companion. We argue, however, that the available data support the first scenario.

Key words: stars: individual (HD110432) – X-rays: binaries

Online-only material: color figures

1. INTRODUCTION

Until recently, γ Cas (B0.5IVe) stood alone as the major exception to our understanding of the X-ray emission from massive stars. Its X-ray spectrum is dominated by very hot ($kT \simeq 10$ keV) thermal emission at an X-ray luminosity of $\sim 10^{32}$ erg s^{-1} in the 2–20 keV energy band, comparable to the brightest OB stars, much less than typical Be X-ray binaries ($\sim 10^{35-37}$ erg s^{-1}) and even below low-luminosity ($\sim 10^{33-35}$ erg s^{-1}) high-mass X-ray binaries (HMXBs) such as X Per (La Palombara & Mereghetti 2007), SAX J1324.4−6200, and SAX J1452.8−5949 (Kaur et al. 2009). In γ Cas, the leading hypothesis for many years was accretion onto a degenerate companion, most probably a white dwarf (WD; Kubo et al. 1998; Owens et al. 1999). Evolutionary calculations have shown that there should be a large number of binary systems with WD accretors (Waters et al. 1989; Raguzova 2001). These systems would show far-ultraviolet emission and should be observable as low-luminosity X-ray emitters ($L_X \sim 10^{32}$ erg s^{-1}). To date, however, no actively accreting Be + white dwarf (Be + WD)

system has been convincingly identified (see, however, Sturm et al. 2012).

In the past years, a growing number of γ Cas analogs have been identified among late O and early B emission line stars, leading to the definition of a new class of objects: HD110432 (B0.5IIIe; Torrejón & Orr 2001; Lopes de Oliveira et al. 2007), HD119682 (B0.5Ve; Rakowski et al. 2006; Safi-Harb et al. 2007), HD161103 (B0.5e), SAO49725 (B0.5e), NGC 6649 (B1.5e), SS397 (B0.5e; Lopes de Oliveira et al. 2006), and HD157832 (B1.5V; Lopes de Oliveira & Motch 2011). As illustrated by Motch et al. (2007), γ Cas analogs share a very narrow range of optical and X-ray properties: spectral types from B0.5 to B1.5, slightly evolved, moderate and variable X-ray luminosities (of the order of 10^{32} erg s^{-1} in the 0.2–12 keV range) dominated by very hot ($\simeq 10$ keV) thermal plasmas, and extended circumstellar disks Hα emissions with EW(Hα) ~ 30–40 Å. None of them, except γ Cas, have so far shown any sign of binarity. γ Cas is now known to be a wide binary. Its X-ray emission, however is devoid of any coherent modulation, orbital or otherwise.

The nature of this X-ray emission remains a mystery. Two mechanisms have been proposed: in general, the broadband X-ray spectrum is reminiscent of cataclysmic variables. The accretion onto a WD provides a natural explanation for the hot thermal emission (as opposed to the power law displayed by NS systems in HMXB), while the smaller potential well of the WD accounts naturally for the lower luminosity. This picture, however, has some difficulties fitting into our current understanding of stellar and binary evolution. Indeed, the progenitor of the WD should have been more massive than the (early) Be star and it is by no means clear how a massive star of 20 $M_\odot$ can end as a WD. In the case of HD110432, no binary companion is known either. A tentative periodic pulsation of 14 ks was claimed by Torrejón & Orr (2001) using a *BeppoSAX* observation. Later, however, Lopes de Oliveira et al. (2007) found no evidence of such a pulsation, nor any other, in an extensive analysis of three *XMM-Newton* observations. On the other hand, γ Cas is now known to be a wide binary with a $\sim$1 $M_\odot$ star in a 203.59 day period orbit (Harmanec et al. 2000). This makes accretion very inefficient. According to current simulations (Okazaki et al. 2002), it is not possible to completely exclude the hypothesis in which matter is channeled in arm oscillations toward the (tentative) companion. Even in such a case, the WD would be more likely in a circular orbit truncating the disk, which renders the accretion mechanism more inefficient to explain the X-ray emission.

The alternative explanation is magnetic-disk–Be star interaction (Robinson et al. 2002; Smith et al. 2004; Smith & Balona 2006). This model can explain not only the X-ray properties, but also the related UV and optical signatures, without the need to introduce an unseen compact companion. The extremely hot X-ray emitting gas is hypothesized to be entrained in a tangled magnetic field which also produces soft X-rays from flare/disk–cloud interactions as well as cold fluorescence from the disk. This interpretation, however, poses serious challenges to the theory. A key ingredient is the presence of a magnetic field, and it is by no means clear how such a field could be produced and sustained in the radiative mantle of an OB star. Despite this, there is now a growing number of early-type stars where the magnetic field has been detected and measured, for example, θ^1 Ori C (Donati et al. 2002), HD108 (Martins et al. 2010), τ Sco (Donati et al. 2006b), and HD191612 (Donati et al. 2006a). On the other hand, other Be stars, with similar spectral types and comparably large disks, do not show any X-ray emission at all. In either case, our current understanding of stellar and binary structure and evolution will be challenged. To characterize and understand the class of γ Cas analogs is, therefore, very important.

In this work, we present an analysis of a *Chandra* gratings observation of the Be X-ray source HD110432 (1H1249−637 = BZ Cru, B0.5IIIe). Torrejón & Orr (2001, hereinafter TO01) performed an analysis of *BeppoSAX* data describing the spectrum in terms of an optically thin thermal plasma at 10.55 keV. This was interpreted under the Be + WD scenario. The similarity of this system with γ Cas was first noted by Robinson et al. (2002). Smith & Balona (2006) performed an extensive analysis of optical data which supported the magnetically active star hypothesis, and definitely established the similarity with γ Cas. Later, Lopes de Oliveira et al. (2007, hereinafter LO07), in an extensive analysis of *XMM-Newton* PN and MOS data at CCD resolution, found that the correct description of the system required several optically thin thermal plasmas of different temperatures and, perhaps, different absorption columns. The source spectrum was found

to vary strongly in time. Again, the X-ray behavior is reminiscent of that of γ Cas but the true nature of the object (whether single active Be star or Be binary) remains elusive. In order to shed new light on the nature of the system, we performed a 141 ks pointed observation of HD110432 with *Chandra* gratings. This observation represents the highest resolution X-ray spectrum ever taken for a γ Cas analog as well as the longest uninterrupted light curve of HD110432 performed so far. In order to complement our understanding of the underlying broadband continuum, we have also used a 25 ks *Suzaku* X-ray Imaging Spectrometer (XIS) and Hard X-ray Detector (HXD) observation taken from the public archive.

2. OBSERVATIONS

2.1. Chandra HETG Data

We have processed and analyzed the *Chandra* data from the ObsID 9947. The High Energy Transmission Gratings (HETG) spectrometer (Canizares et al. 2005) acquired data during a total of 141.28 ks. Both High Energy Gratings (HEG; 1.55–17.7 Å) and Medium Energy Gratings (MEG; 1.55–31 Å) were used for the analysis. After excluding wavelength ranges with insufficient signal, we obtained spectral coverage from 1.6 to 16 Å. The spectra and the response files (arf and rmf) were extracted using standard procedures with the CIAO software (ver. 4.4). The data were binned to match the resolution of HEG (0.012 Å, FWHM) and MEG (0.023 Å, FWHM) and have a minimum signal-to-noise ratio (S/N) of seven. First dispersion orders ($m = \pm1$) were fitted simultaneously. The peak count rate in a single (MEG) gratings arm spectrum is $\approx$0.04 counts s^{-1} $Å^{-1}$, which is well below the level at which pileup is a concern.[3]

The analysis was performed with the Interactive Spectral Interpretation System (ISIS) version 1.6.1-24 (Houck & Denicola 2000). For the analysis, we use the abundance table from Anders & Grevesse (1989) and cross sections from Balucinska-Church & McCammon (1992).

2.2. Suzaku Data

We have processed and analyzed public data from instruments on board *Suzaku* (Mitsuda et al. 2007). We used standard procedures to reduce the XIS (Koyama et al. 2007) CCD detector (0.3–10 keV) and the HXD (Takahashi et al. 2007). The standard screening criteria (satellite out of the South Atlantic Anomaly, Earth elevation angle >5° and Day-Earth elevation angle >20°) were applied to create the Good Time Intervals (GTI). Events were readout from either 3×3 or 5×5 pixel islands. We created individual spectra and response files for each detector and data mode combination. Response matrices and effective area files were created using the xisrmfgen and xissimarfgen tasks, respectively. All three XIS detectors, XIS 0, 1, and 3, were combined and rebinned to have a minimum S/N of seven (XIS 2 was lost during a micrometeor hit in late 2006).

For the HXD, only data from the PIN diode detector (10–70 keV) presented enough signal to produce a useful spectrum. The PIN data were extracted from the cleaned event files in the hxd/event-cl directories. The source spectra exposure times were corrected with the hxdcorr tool. The PIN spectra were grouped to have an S/N $\geqslant$ 10 in each energy bin. Table 1 presents the journal of the observations with both telescopes.

---

[3] See *The Chandra ABC Guide to Pileup*, v.2.2, http://cxc.harvard.edu/ciao/download/doc/pileup_abc.pdf
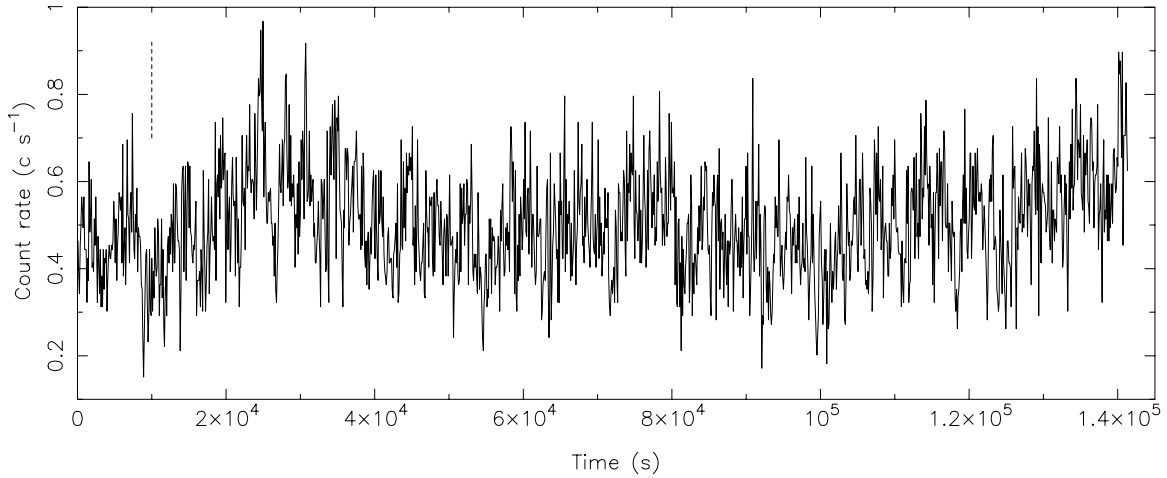
Figure 1. *Chandra* 141 ks light curve, in the 1.6–16 Å wavelength range, rebinned in 100 s intervals. The vertical dashed line in the upper left corner represents the typical error bar per bin.
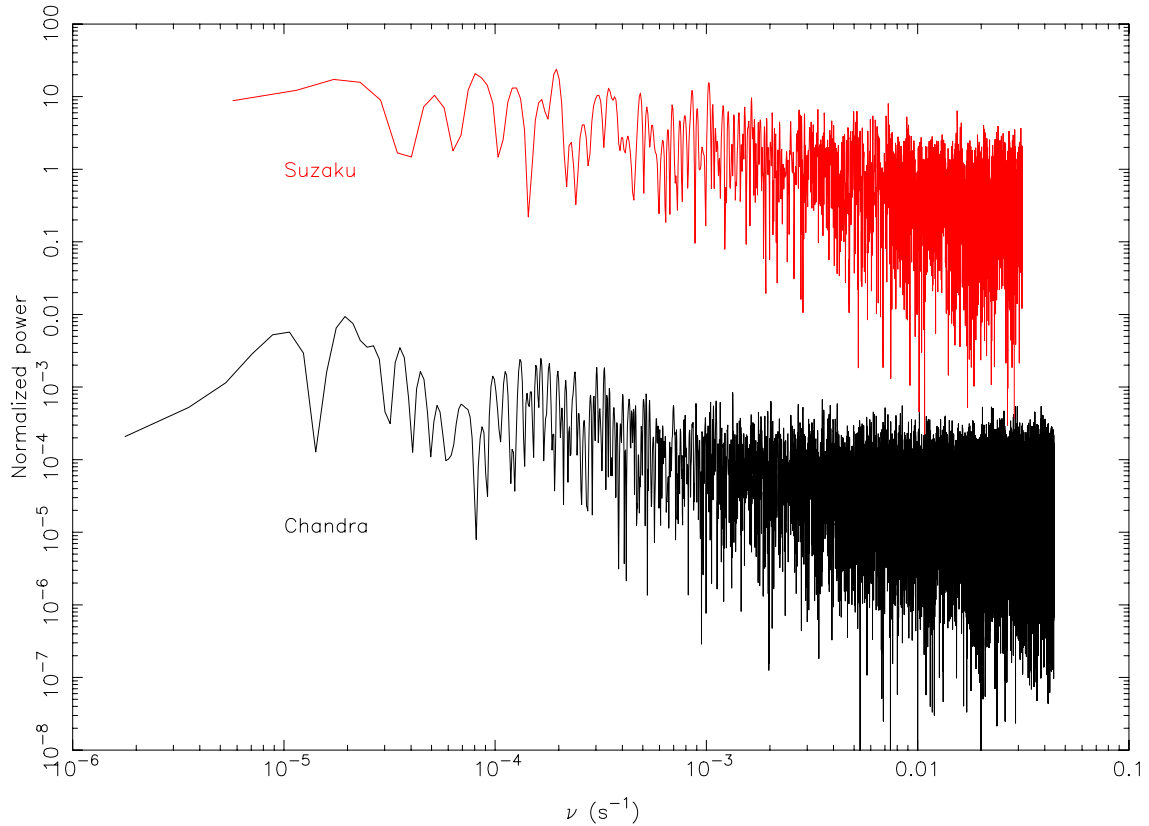
Figure 2. Power spectrum corresponding to the 10 s binned *Chandra* light curve (bottom) and 16 s binned Suzaku light curve (top). No coherent period stands out. In particular, the 14 ks pulsation ($\nu = 7.14 \times 10^{-5}$ Hz) is not detected.

(A color version of this figure is available in the online journal.)

Table 1
Observations Analyzed

Telescope	ObsID	Date	t_{exp} (ks)
Chandra	9947	2009 Nov 13 20:09:37	141.28
Suzaku	403002010	2008 Sep 9 21:45:28	25.33

3. TIMING ANALYSIS

Our 141 ks *Chandra* observation represents the longest uninterrupted observation of this source (in fact, of any γ Cas analog) made so far. This allows us to search for coherent pulsations over a wide range of frequencies. In Figure 1, we present the *Chandra* light curve binned to 100 s bins. Both HEG and MEG have been added and all orders have been used. As can be seen, the source is very variable on short timescales, showing a characteristic flaring pattern. In the long timescale, however, the source seems to lack particularly big flares and looks quite stable. In order to search for coherent pulsations, we have analyzed the light curve with a time resolution of 10 s.[4] In Figure 2 (bottom plot), we show the normalized fast Fourier transform

---

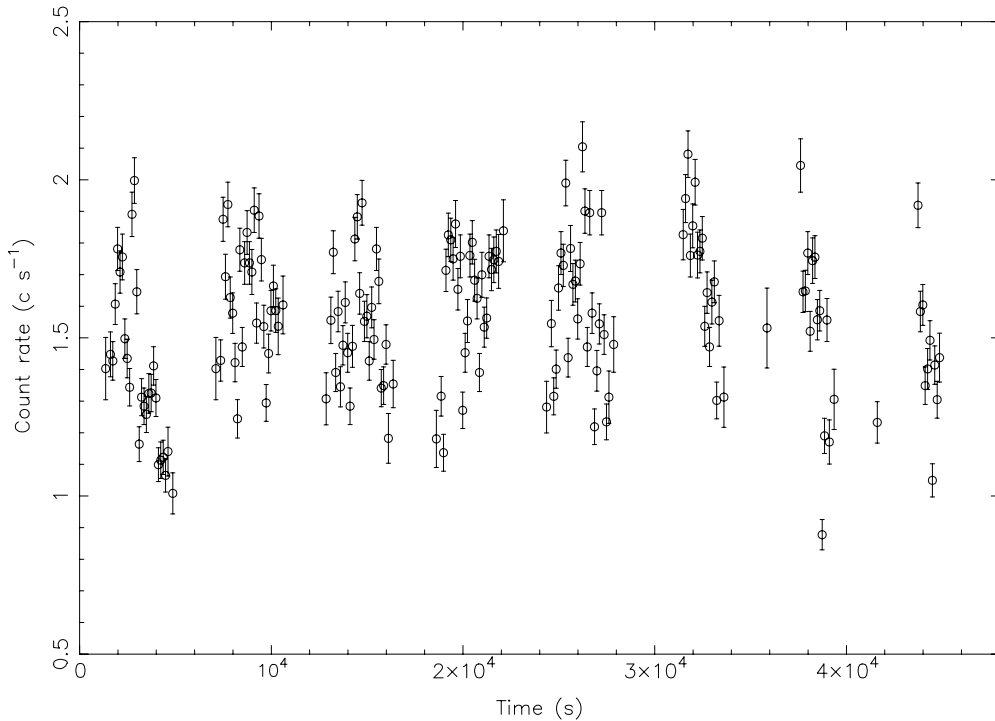[4] The HETG data appeared too noisy with smaller bins.

3

Figure 3. *Suzaku* 20 ks light curve in the 0.5–9 keV band shown in time bins of 200 s.

periodogram of the light curve, using the Lomb–Scargle technique. As can be seen, no significant period stands out. We have performed the same search using larger time bins to reduce errors. We fail to detect any significant period. Torrejón & Orr (2001) suggested the possibility of a 14 ks pulsation in the *BeppoSAX* light curve of HD110432. This detection, however, was rather uncertain because the observation covered just one cycle. Later, Lopes de Oliveira et al. (2007) did not find any pulsation at such a period in any of the three longer *XMM-Newton* EPIC light curves studied. In the present data set, we do not find evidence of any significant period up to the Nyquist frequency (0.05 Hz).

In Figure 3, we show the *Suzaku* 0.5–9 keV XIS light curve in 200 s bins. The light curves shows, again, high variability on short timescales. The corresponding power spectrum is shown in Figure 2 (upper plot) where we have used 16 s time bins. As can be seen, no significant period stands out either. In summary, all attempts made so far to find a coherent period have failed.

In order to explore the hardness variations of the X-ray source, we have extracted the *Chandra* light curves in the wavelength intervals 1.5–3 Å, 3–6 Å, and 6–16 Å, referred to here as hard (H), medium (M), and soft (S) bands, respectively. In Figure 4, we show the variation of medium/high, soft/medium, and soft/high hardness ratios with counts. As can be seen, the source does not present any correlation of hardness ratio with source intensity in any of the energy bands. The points are scattered more or less uniformly around a mean value. The differences between hardness values are, however, significant. In Figure 5, we show the ratio of the hard (1.5–3 Å) to medium/soft energy band (3–16 Å) with the intensity. This plot can be compared with Figure 6 in LO07. Specifically, the behavior during the *Chandra* observation seems to be very similar to the *XMM* observation 1 analyzed by LO07. This reflects the rapid variability of the X-ray energy distribution on short timescales. However, there seem to be no large variations on longer timescales.

4. SPECTRAL ANALYSIS

4.1. Continuum and Physical Models

In previous works on HD110432 (LO07) and γ Cas (Smith et al. 2004; Lopes de Oliveira et al. 2010), it was shown that the description of the spectrum of these sources requires several optically thin thermal plasma components (MEKAL, APEC) to correctly account for both the shape of the continuum and the emission line strengths. One of the critical points left open by LO07 was whether the different plasmas in HD110432 were affected by distinct absorption columns. The high-resolution *Chandra* HETG spectrum will allow us to further investigate this issue. In Figure 6, we show the *Chandra* HETG unfolded spectrum of HD110432.

It has been shown in Torrejón et al. (2010), that the Fe K fluorescence is always accompanied by the presence of a K edge in massive binaries. This edge is produced by those photons energetic enough to ionize the innermost K shell electrons of the atom. This hole is subsequently replenished by an electron from the upper level producing the observed fluorescence line. Consequently, the Fe K edge is deeper than what is imposed by the curvature of the spectrum at low energies. In general, then, all the models will require an additional edge at 1.74 Å (=7.125 keV). We will fix the wavelength and let the optical depth τ vary free. Likewise, all models require the addition of a fluorescence line at 1.9366 Å, compatible with neutral Fe (I to VIII) from the illumination of cold material or reflection onto the tentative WD. This line is not included in the plasma models.

As can be seen in Table 5, the emission lines present in the *Chandra* spectrum trace a range of plasma temperatures. We have tried a single thermal component modified by a single absorption column, using the vmekal model. As expected, this model does not produce a good fit to the continuum, especially at low energies. The reduced $\chi_r^2 = 1.46$ for 938 degrees of freedom (dof). In order to account for the soft excess, and in agreement with LO07, we find that at least three plasmas, at
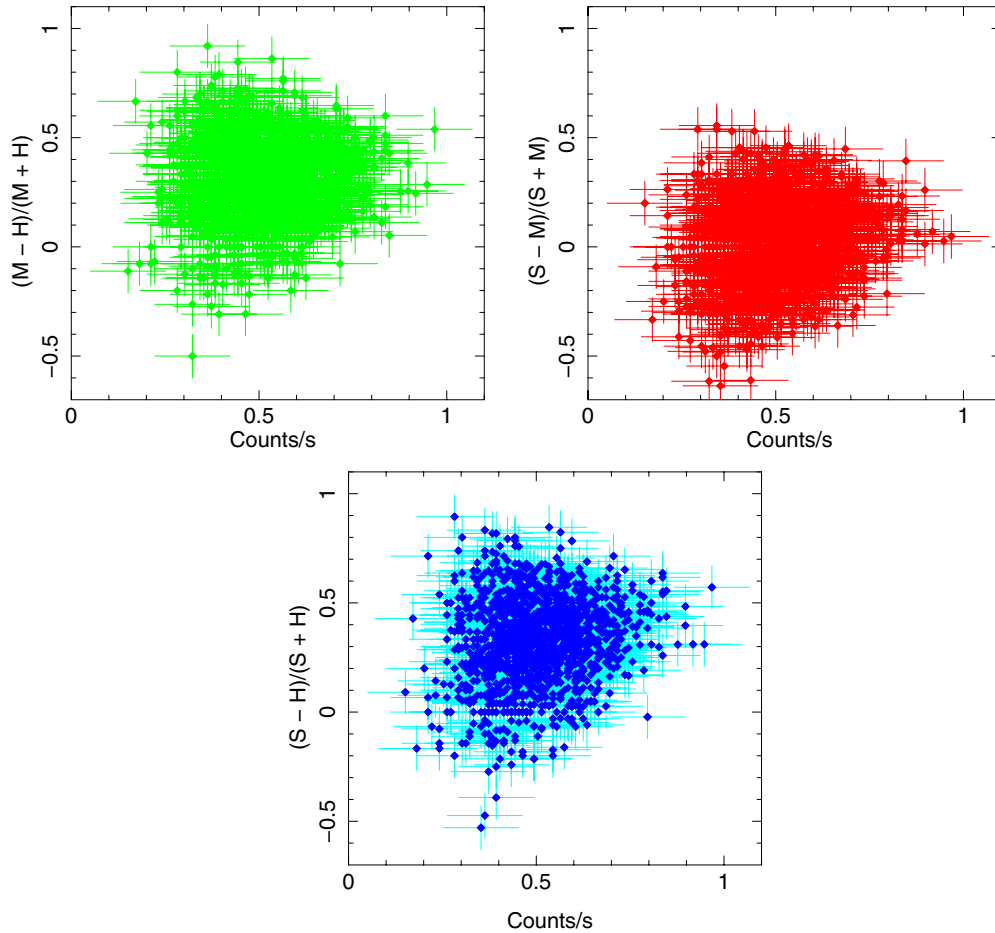
Figure 4. *Chandra* color–color plots for several combination of hardness ratios: medium/high, soft/medium, and soft/high.
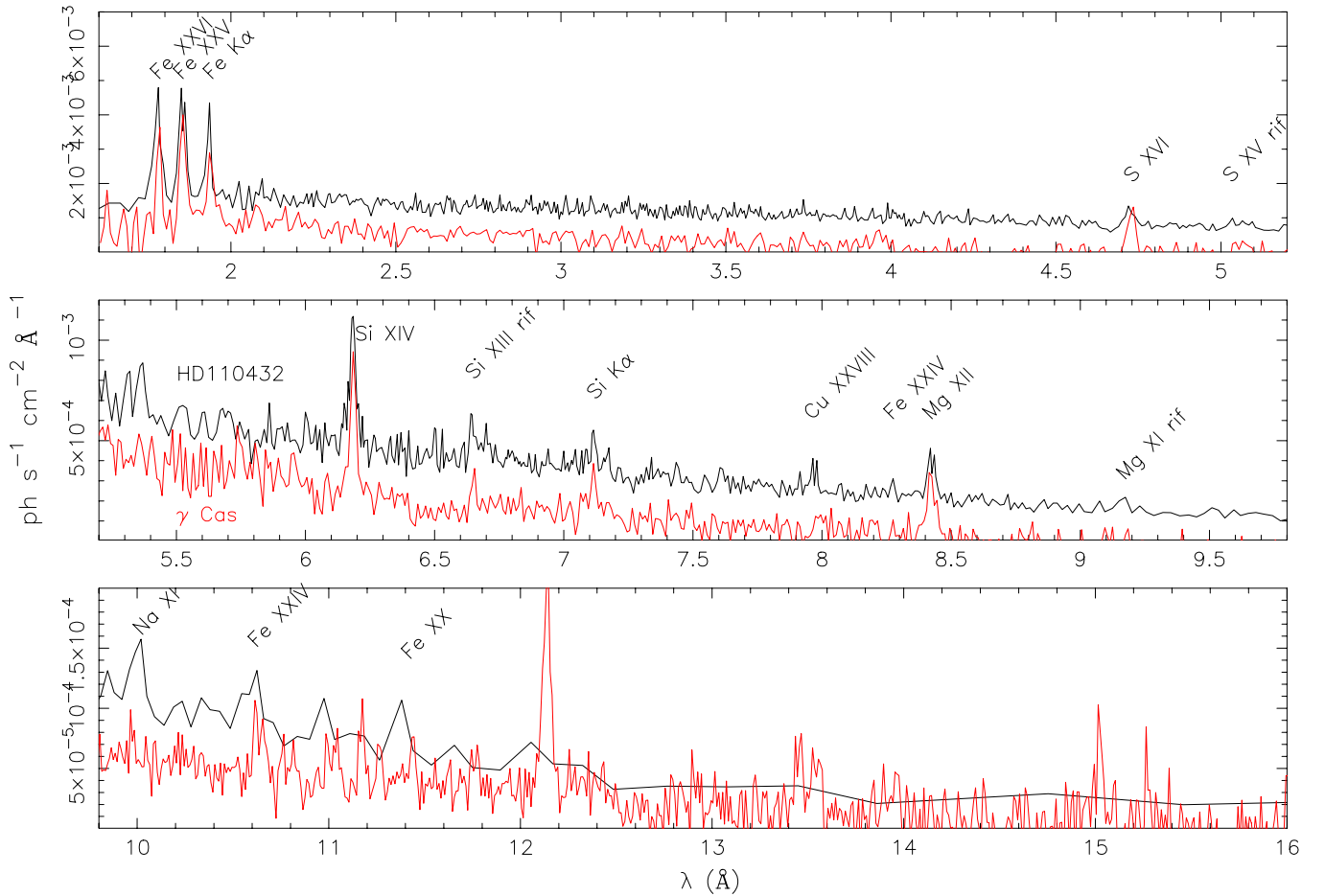(A color version of this figure is available in the online journal.)
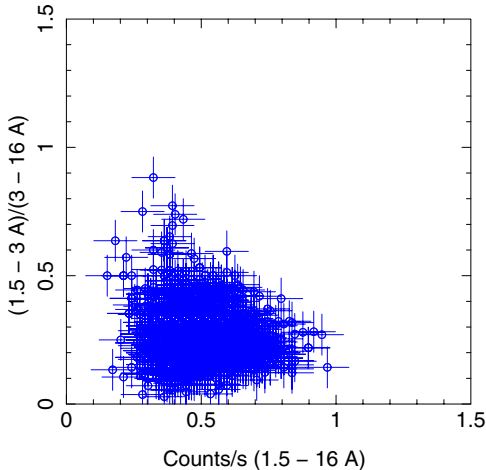
Figure 5. *Chandra* color–magnitude diagram. Color is defined as the flux ratio between intervals (1.5–3 Å)/(3–16 Å).

(A color version of this figure is available in the online journal.)

different temperatures, are required. However, using a single absorption column to modify all three thermal components yields a reduced $\chi_r^2 = 1.25$ for 935 dof. The most evident discrepancies are still in the low energy continuum. In order to properly describe the whole *continuum*, we find that three distinct absorption columns must be used to modify each of the

three `vmekal` components. The fit improves significantly. The reduced chi square is now $\chi_r^2 = 1.19$ for 933 dof. An *F* test gives a statistic value of $F = 23.5$, and the probability for the addition of the individual absorptions not being significant is only 1.08×10^{-10}. At this point, the continuum is fairly well described both at high and at low energies by three optically thin thermal plasmas at $kT \approx 22$, 8, and 0.2 keV, respectively. Following previous works, we will call them *hot*, *warm*, and *cool* plasmas, respectively. The overall Fe abundance is 0.48 solar. The main discrepancies are now in the line strengths. In particular, it is evident that the Fe L shell transitions (Fe XXIV, Fe XX) that dominate the low energy spectral range are severely underestimated by this model. Therefore, we next investigated the elemental abundances in the several plasmas by letting the Fe abundance to vary independently. We find that the abundance of the hot component is subsolar while the abundances of the warm and cool components are compatible between them. Therefore, we tie the abundances in the warm and cool components and let the abundance in the hot component vary freely. The best-fit parameters are shown in Table 2, under the Model 2 column. Owing to the normalization of the several components, the hot plasma dominates the spectrum, followed by the warm and cool plasmas, respectively. The absorption columns follow this hierarchy as well. The absorption for the cool component turns out to be very low. We have fixed it to the interstellar medium (ISM) value ($N_H \approx 0.15 \times 10^{22}$ cm^{-2}). The Fe abundance is subsolar. However, the Fe abundance of the hot component

Figure 6. *Chandra* HETG unfolded spectrum of HD110432 (top, black) analyzed in this work. The HETG spectrum of γ Cas, presented in Smith et al. (2004), is also shown (bottom, red) scaled and offset for comparison.

(A color version of this figure is available in the online journal.)

($Z_{\rm Fe} = 0.30\,Z_\odot$) is significantly lower than for the warm and cool components ($Z_{\rm Fe} = 0.76\,Z_\odot$), which turn out to be equal within the errors and to have been tied during the fittings.

In Figure 7, we plot the unfolded spectrum with the three vmekal composite model. In the first three panels, we show the resulting fit for the continuum and the lines, while in the fourth panel we show the individual contributions of each component. The reduced $\chi_r^2 = 1.07$ for 932 dof. As can be seen, the continuum is well accounted for but some discrepancies still exist in the lines. Two cases stand out. First, the observed strength of the Na XI Lyα line at 10.02 Å is much stronger than predicted by the model using solar abundance. We let it vary freely, keeping it tied for the three components. The resulting Na abundance is very high ([$\sim$15 $\pm$ 5] $Z_\odot$). Unfortunately, the spectrum starts to be noisy at these wavelengths, but a high Na abundance seems to be necessary to correctly fit the line. Second, the peak emission of the Fe XXVI Lyα and Fe XXVI lines, at 1.78 and 1.86 Å, respectively, seems slightly overpredicted, while the observed profiles are definitely broader than the model. Therefore, the next step is to modify the width of the observed lines with the effects of turbulent velocity. For that purpose, we use the bvapec model, for collisionally ionized plasma based on the *Astrophysical Plasma Emission Code* (APEC).

In Table 2, under the Model 3 column, we show the corresponding fit parameters. The hierarchy of normalizations and absorptions is still observed. The temperatures of the hot and warm components are lower, $kT = 16.3$ and 7.1 keV, respectively, while the temperature of the cool component is a bit higher, $kT = 0.28$ keV, although its norm is smaller than in the previous model.

In Figure 8, we show the unfolded spectrum for this model. As can be seen, both Fe XXVI and Fe XXV are much better described now. These two lines are the main contributors, within the investigated spectral range, to the $v_{\rm turb}$ determination. The required $v_{\rm turb}$ is of the order of 1200 km s^{-1}. No turbulent broadening is needed to modify the warm and cool components. Note, however, that the Mg (9.2 Å) and Na (10.02 Å) lines are underestimated. The bvapec model does not have the Na abundance as variable and cannot fit it well. This reinforces the conclusion from the previous analysis that the Na seems to be highly abundant. However, the reduced $\chi_r^2 = 1.04$ for 931 dof is the best we have found in our analysis. It is plausible that a correct description of the whole spectrum will be a hybrid collisional/photoionized plasma. In the last panel of Figure 8, we show the relative contribution of the several plasmas. The prominent S XVI, Si XIV, and Mg XII lines as well as the Fe L shell transitions are contributed mainly by the $kT = (8-9)$ keV plasma. Although it also contributes to Fe XXV and Fe XXV lines, these are dominated by the hot component. Finally, the $kT = 0.3$ keV cool plasma contributes significantly only beyond $\lambda \sim 12$ Å.

Table 2
Model Parameters for *Chandra* Data Only

Component	Parameter	Value		
		Model 1	Model 2	Model 3
Edge	E (keV)	7.125[a]	7.125[a]	7.125[a]
	τ	$0.23^{+0.15}_{-0.10}$	$0.25^{+0.13}_{-0.10}$	$0.19^{+0.14}_{-0.11}$
Power law	N_H[b]	$3.04^{+0.15}_{-0.04}$	...	...
	Norm	$0.005^{+0.002}_{-0.001}$	...	...
	Γ	$1.56^{+0.005}_{-0.10}$	...	...
Thermal (hot)	N_H	...	2.09 ± 0.29	2.25 ± 0.12
	Norm	...	0.023 ± 0.002	0.024 ± 0.004
	kT (keV)	...	22^{+8}_{-5}	16^{+5}_{-2}
	Z_{Fe}	...	0.30 ± 0.12	0.32 ± 0.15
	v_{turb} (km s^{-1})	...	...	1200 ± 300
Thermal (warm)	N_H	0.89 ± 0.10	0.72 ± 0.12	0.70 ± 0.13
	Norm	$0.017^{+0.006}_{-0.002}$	$0.0104^{+0.0010}_{-0.0005}$	0.011 ± 0.0003
	kT (keV)	8.82 ± 0.75	$8.07^{+0.80}_{-0.88}$	7.11 ± 0.83
	Z_{Fe}	0.68 ± 0.15	0.76 ± 0.20	0.75 ± 0.13
Thermal (cool)	N_H	0.17 ± 0.05	0.15[c]	0.15[c]
	Norm	0.0006 ± 0.0002	0.0006 ± 0.0005	0.00017 ± 0.0005
	kT (keV)	0.20 ± 0.08	0.19 ± 0.03	0.28 ± 0.07
	Z_{Fe}	0.68 ± 0.15	0.76 ± 0.20	0.75 ± 0.13
	Flux[d]	3.78	3.78	3.78
Fe Kα	λ	$1.9365^{+0.0005}_{-0.0004}$	$1.9366^{+0.0005}_{-0.0004}$	$1.9366^{+0.0005}_{-0.0004}$
	Flux[d]	3.72 ± 0.55	4.14 ± 0.22	4.23 ± 0.23
EW (eV mÅ^{-1})		88.76/26.84	83.92/25.34	89.32/27.01
	χ^2_r (dof)	1.07 (932)	1.07 (932)	1.05 (932)

Notes. Model 1: PO+2 VMEKAL; Model 2: 3 VMEKAL; Model 3: 3 BVAPEC.
[a] Fixed.
[b] All N in units of $\times 10^{22}$ cm^{-2}.
[c] Fixed at the interstellar value.
[d] Unabsorbed total flux in units of $\times 10^{-11}$ erg s^{-1} cm^{-2}.

Given the limited *Chandra* bandpass, it is necessary to check the consistency of the hard tail with a hot (thermal or no-thermal) emission. Indeed, at such high temperatures, a thin plasma already displays a power-law shape at the energies considered here. To that end, we substitute the hot component by an absorbed power law. The fit is also good and the parameters are given in Table 2, under the Model 1 column. The most significant change is the increase in the norm of the warm component, which is now dominant. The main discrepancy between the data and the model is, again, in the line strengths. Fe xxv (1.85 Å) is overestimated while Fe xx (11.4 Å) is underestimated. In terms of the χ^2_r and fit to the continuum, however, this model works equally well.

In order to try to break down this degeneracy, we have tried to establish the underlying broadband continuum using *Suzaku*. In Figure 9, we present the combined XIS and HXD *Suzaku* data fitted with three optically thin thermal plasmas. Significant emission is seen up to, at least, 33.5 keV, even though the number of energy bins is very low at high energies. In the *BeppoSAX* data presented in TO01, this hard tail could be seen up to 50 keV. The S/N of the PDS data on board *BeppoSAX* was, unfortunately, also low. However, a hard tail is definitely established for this system. Consistent with the previous discussion, the *Suzaku* data can be modeled with either a sum of thermal plasmas or a thermal-power-law mixture. The *Suzaku* data, however, do not require the cooler component. In Table 3, we present the details of the fit to the *Suzaku* data only. As can be seen in Tables 2 (Models 2 and 3) and 3 (Model 2), for pure thermal models, the source exhibits a complex variability, a fact already

Table 3
Model Parameters for *Suzaku* Data Only

| Component	Parameter	Value	
		Model 1	Model 2
Power law	$N_H (\times 10^{22}$ cm$^{-2})$	2.94 ± 0.23	...
	Norm	0.0036 ± 0.0009	...
	Γ	$1.58^{+0.10}_{-0.02}$	...
Thermal (hot)	$N_H (\times 10^{22}$ cm$^{-2})$	...	2.12 ± 0.23
	Norm	...	0.015 ± 0.005
	kT (keV)	...	33^{+3}_{-5}
	Abundance	...	0.20 ± 0.25
Thermal (warm)	$N_H (\times 10^{22}$ cm$^{-2})$	0.47 ± 0.22	0.44 ± 0.23
	Norm	0.018 ± 0.001	0.017 ± 0.001
	kT (keV)	9.44 ± 0.12	8.69 ± 0.13
	Abundance	0.73 ± 0.23	0.71 ± 0.25
	Flux[a]	3.74 ± 0.13	3.75 ± 0.13
Fe Kα	λ	1.938 ± 0.002	1.938 ± 0.002
	FWHM	$\leqslant 5$ mÅ[d]	$\leqslant 5$ mÅ[d]
	EW (mÅ)	29.20	30.2
	Flux[e]	4.26	3.58
	χ^2_r (dof)	1.304 (190)	1.295 (189)

Notes. Model 1: po+Mekal, Model 2: 2 Mekal.
[a] $\times 10^{-11}$ erg s^{-1} cm^{-2}; [0.78–8.27] keV = [1.5–16] Å.
[b] Fixed.
[c] $\times 10^{-5}$ photons s^{-1} cm^{-2}.

noted by LO07. The hot component is hotter during the *Suzaku* observation while the temperature of the warm component is
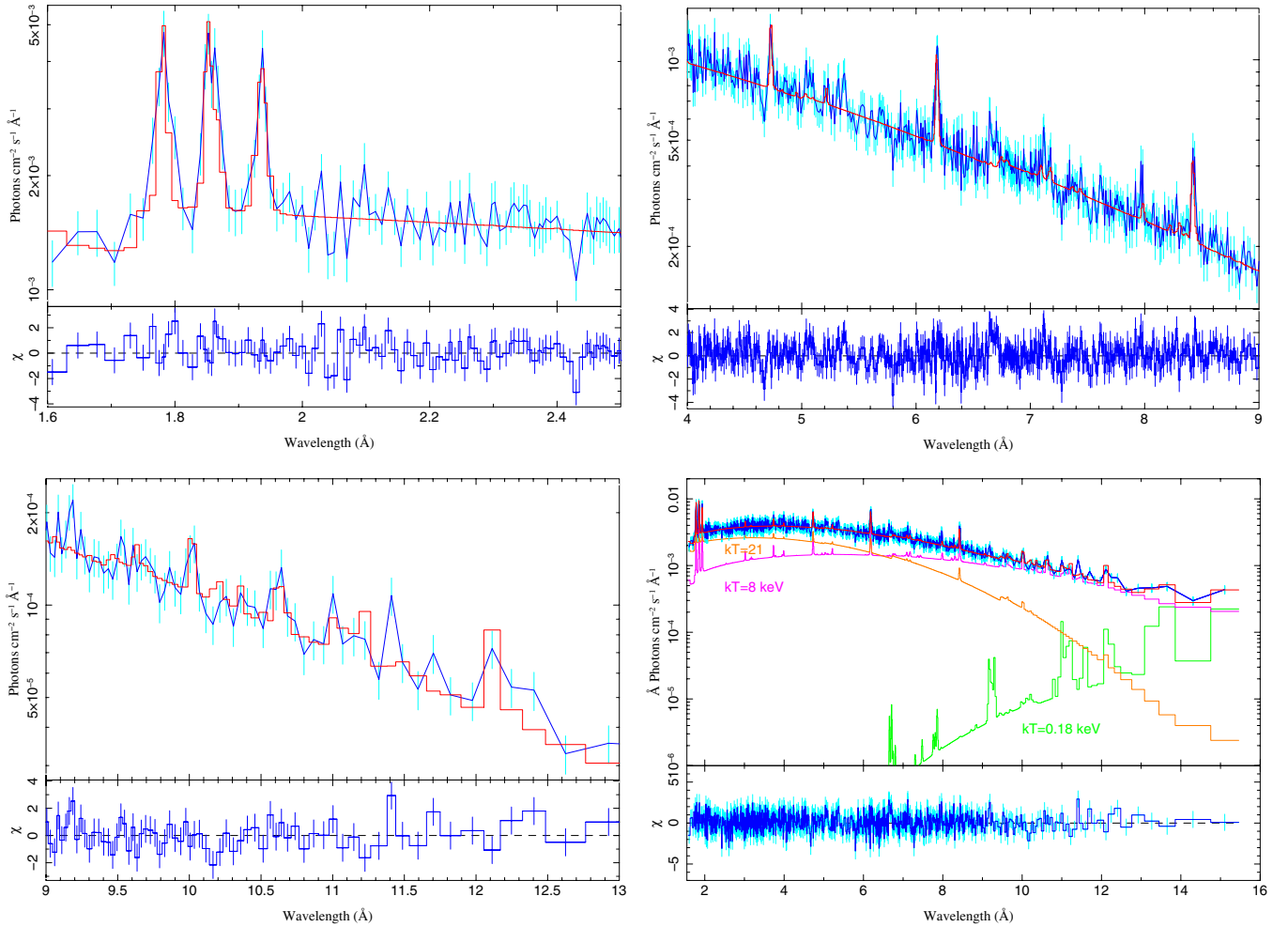
Figure 7. *Chandra* HETG unfolded spectrum of HD110432 with the `vmekal` model fit in the wavelength intervals 1.5–2.5 Å, 4–9 Å, and 9–13 Å. The fit in the Fe line complex region is not as good as with the collisional plasma model. The exact values of the plasma temperatures are quoted in Table 2.
(A color version of this figure is available in the online journal.)

similar. However, the norm of the hot and warm component was lower and higher, respectively, during the *Suzaku* observation. In the case of the thermal plasma + power-law model, the most noticeable change is in the norm of the power law which again was less important here than during the *Chandra* observation. This precludes any attempt to obtain physical parameters based on the joint fit to both data sets. Unfortunately, the low S/N of the *Suzaku* HXD data does not allow us to determine its full extension. The goodness of the fit is comparably good for both models. We cannot unambiguously constrain the very nature of the hard component with the available data sets and hence further observations will be required to establish this point.

4.2. Cooling Flow Model

One of the fingerprints of accretion on to the WD in some cataclysmic variables is through the cooling of the post-shock X-ray plasma (see, for example, Mukai et al. 2003). In order to test this scenario, we have tried to fit the cooling flow model `cemekl` to the *Chandra* data. A single absorbed `cemekl` component does not fit the data at all. An acceptable fit is obtained with the addition of a power law. The best-fit parameters are displayed in Table 4. As can be seen, the maximum temperature displayed by the plasma is very high (∼37 keV), and the α parameter is close to the adiabatic case

Table 4
Model Parameters for the Cooling Flow Model Fit to *Chandra* Data

| Component	Parameter	Value
Edge	E (keV)	7.125[a]
	τ	0.42 ± 0.02
Power law	$N_{\rm H}(\times 10^{22}\ {\rm cm}^{-2})$	1.18 ± 0.23
	Norm	0.0026 ± 0.0009
	Γ	$1.13^{+0.10}_{-0.02}$
Thermal	Norm	0.027 ± 0.003
	α	0.82 ± 0.10
	$kT_{\rm max}$ (keV)	37.35 ± 0.52
	Abundance	1.26 ± 0.23
Fe Kα	λ	1.938 ± 0.002
	Flux[c]	3.74
	FWHM	$\leqslant 5$ mÅ[a]
	EW (mÅ)	21.15
	χ^2_r (dof)	1.24 (936)

Notes. Model: POWERLAW + CEMEKL.
[a] Fixed.
[b] $\times 10^{-5}$ photons s^{-1} cm^{-2}.

($\alpha = 1$). These parameters are consistent with those found by LO07 for the same model. The photon index of the power law is identical. This model, however, gives a much higher
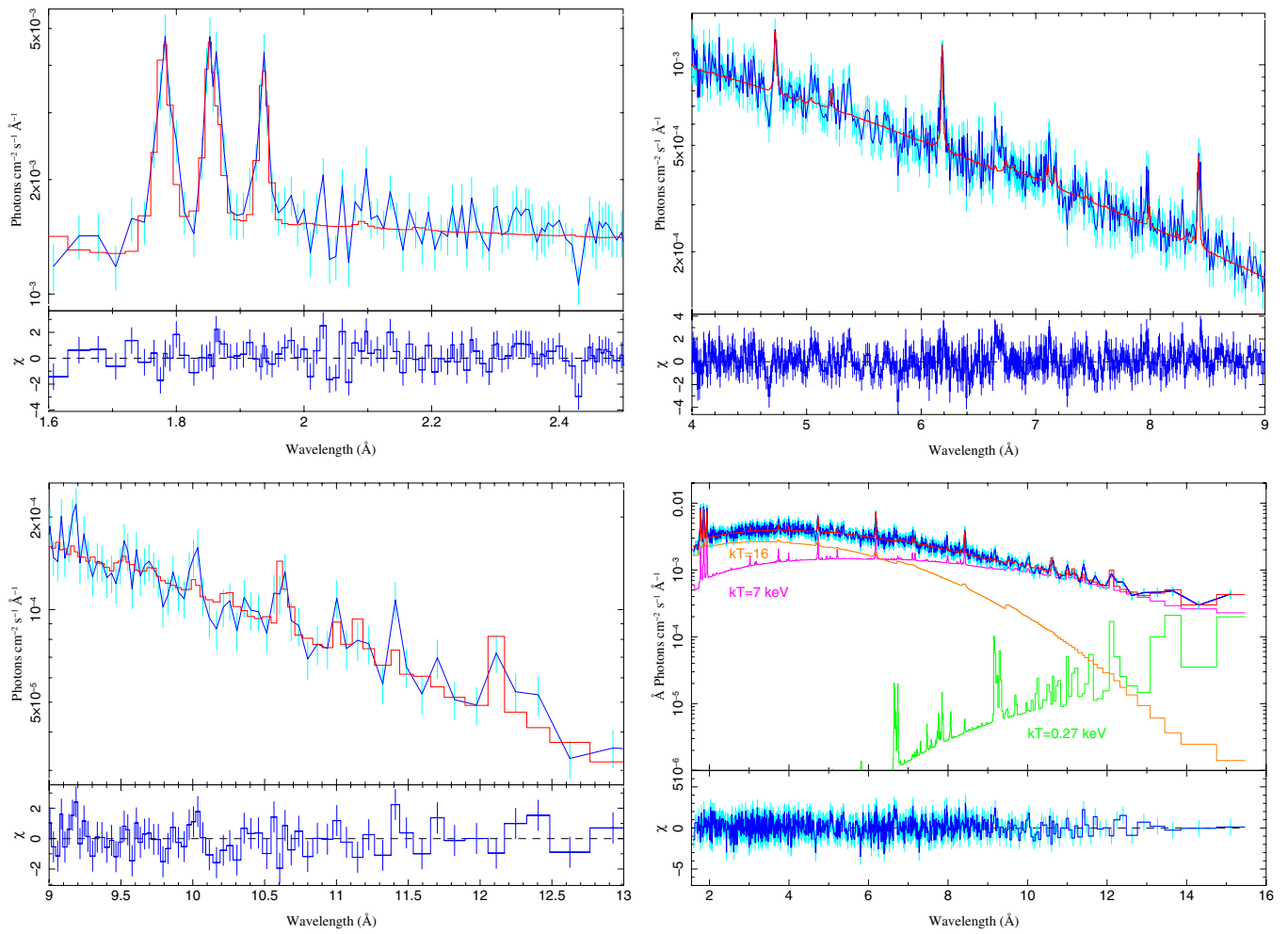
Figure 8. *Chandra* HETG unfolded spectrum of HD110432 with the `bvapec` model fit in the wavelength intervals 1.5–2.5 Å, 4–9 Å, and 9–13 Å. The fit in the Fe line complex region is the best as it accounts simultaneously for the abundance and v_{turb} effects. In the low energy tail, the Na XI line at 10.02 Å is not fitted properly since the abundance of this element cannot be set within this model. The exact values of the plasma temperatures are quoted in Table 2.

(A color version of this figure is available in the online journal.)
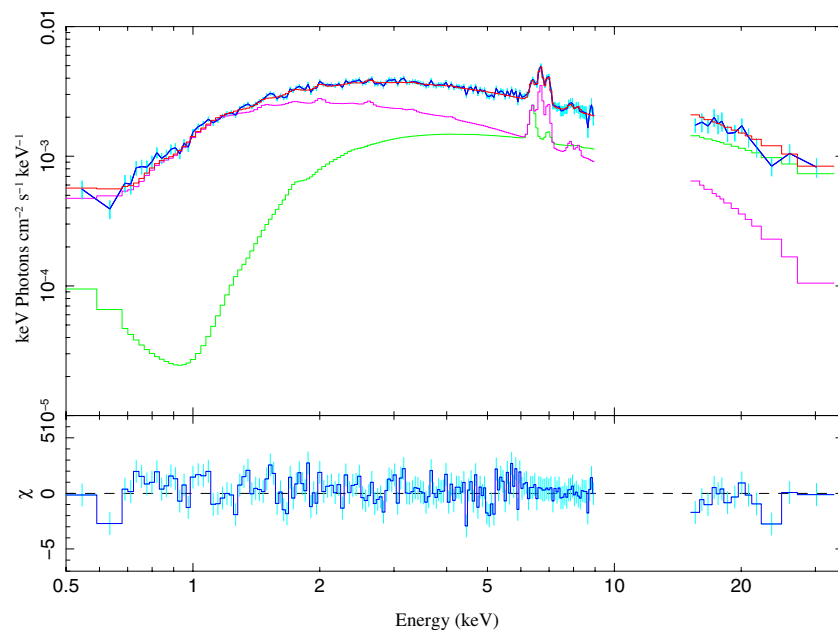
Figure 9. *Suzaku* XIS and HXD spectra of HD110432 fitted with a two thin thermal plasmas modeled with `vmekal`. The parameters for two `bvapec` components are very similar.

(A color version of this figure is available in the online journal.)

Table 5
Emission Lines Identified in the *Chandra* Spectrum of HD110432

Ion	λ	Flux $\times 10^{-6}$	σ	EW	kT_{max}	EM $\times 10^{55}$
	(Å)	(ph s^{-1} cm^{-2})	(Å)	(mÅ)	(keV)	(cm^{-3})
Fe XXVI Lyα	1.7821 ± 0.0020	71.09 ± 14	0.0098 ± 0.0032	44.94 ± 8.86	10.85	6.42 ± 1.26
Fe XXV	1.8550 ± 0.0025	75.90 ± 12	0.0088 ± 0.0030	48.42 ± 7.70	5.43	5.98 ± 0.92
Fe Kα	$1.9366^{+0.005}_{-0.004}$	$41.95^{+1.20}_{-0.30}$	0.005	27.09 ± 0.33	...	...
S XVI Lyα	4.7287 ± 0.0015	$16.04^{+0.7}_{-0.5}$	0.010 ± 0.0020	20.49 ± 0.77	2.17	1.62 ± 0.06
S XV r	5.0387^a	5.10 ± 2.48	0.005	5.58 ± 2.71	1.37	0.14 ± 0.07
S XV i	5.0665^a	3.73 ± 1.53	0.005	4.62	...	...
S XV f	5.1015^a	3.21 ± 1.55	0.005	3.49	...	...
Si XIV Lyα	$6.1856^{+0.021}_{-0.022}$	$19.78^{+0.45}_{-0.10}$	0.0107 ± 0.0020	41.39 ± 0.76	1.37	0.75 ± 0.01
Si XIII r	6.6479	4.88 ± 1.74	0.005	12.67 ± 4.52	0.86	0.06 ± 0.02
Si XIII i	6.6850	2.50 ± 1.55	0.005	7.06	...	...
Si XIII f	6.7395	1.04 ± 0.48	0.005	1.86	...	...
Si Kα	$7.1186^{+0.0001}_{-0.0010}$	4.26 ± 0.20	0.005	12.02 ± 0.56	0.86	...
Cu XXVIII	$7.9667^{+0.008}_{-0.009}$	$2.18^{+0.21}_{-0.07}$	0.005	8.82 ± 0.57		
Fe XXIV	$8.2783^{+0.008}_{-0.007}$	$2.04^{+0.15}_{-0.05}$	0.005	9.43 ± 0.46	1.72	0.02 ± 0.001
Mg XII Lyα	8.4279 ± 0.0032	$8.42^{+0.17}_{-0.30}$	$0.015^{+0.001}_{-0.0002}$	41.74 ± 1.14	0.86	0.24 ± 0.007
Mg XI r	9.1687	2.17 ± 1.44	0.005	16.74 ± 10	0.54	0.03 ± 0.01
Mg XI i	9.2300	0.52 ± 0.25	0.005	6.13 ± 2.92	...	...
Mg XI f	9.3136	0	0.005	0	...	...
Na XI Lyα	$10.0214^{+0.033}_{-0.019}$	$2.50^{+0.22}_{-0.22}$	0.005	22.42 ± 1.79	0.69	1.18 ± 0.09
Fe XXIV	$10.6279^{+0.035}_{-0.022}$	$2.53^{+0.17}_{-0.20}$	0.005	28.92 ± 2.06	1.72	0.02 ± 0.001
Fe XX	$11.4237^{+0.043}_{-0.020}$	$2.62^{+0.17}_{-0.18}$	0.005	40.13 ± 2.76	0.86	2.57 ± 0.18

Notes. Numbers without errors are fixed to the quoted value.
^{a} Fixed.

$\chi^2_r = 1.24$ for 936 dof, than the models discussed in the previous section. The main discrepancies here are in the fit to the low energy continuum as well as the Fe XXVI Lyα line, which is overestimated. We also tried other combinations like `cemekl+mekal`, but the quality of the fit does not improve over the one presented here.
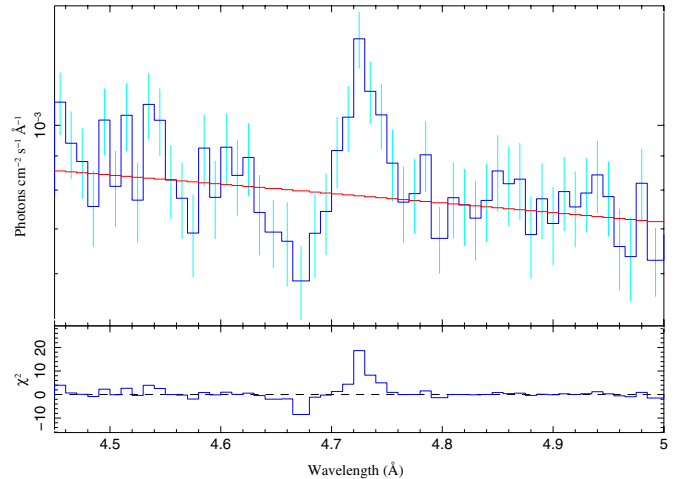
4.3. Emission Lines

In Figure 6, we show the *Chandra* HETG spectrum of HD110432. Below (in red), we have plotted the HETG spectrum of γ Cas analyzed in Smith et al. (2004), in the same wavelength interval, scaled and offset to allow comparison. In general terms, the spectra of both objects are very similar. There are, however, some noticeable differences. Evidently, the Fe XXVI line is much broader in HD110432 than in γ Cas. The Na XI is much stronger in HD110432. Despite the lower S/N of the HD110432 spectrum, it seems evident that the Ne lines at 12.13 and 13.5 Å, respectively, are much stronger in γ Cas. The same seems to be true for the Fe XVII lines around 15 Å.

The spectrum of HD110432 shows a wealth of emission lines available for plasma diagnostics, including the Fe Kα fluorescence at 1.94 Å. To extract their individual parameters, every line was fitted with Gaussians upon a three bremsstrahlung continuum, following the analysis made in the previous sections. Some lines remain unresolved. In such cases, we fixed the line width to $\sigma = 0.005$ Å. The measured equivalent width (EW), though, was found to be independent of this value. All identified and analyzed lines are listed in Table 5.

In the sixth column, we quote the temperature at which the emissivity of the ion is maximum (kT_{max}), taken from the ATOMDB[5] database. This temperature, however, does not necessarily reflect the temperature of the emitting plasma.

Figure 10. S XVI 4.73 Å line presenting a possible P Cygni profile.
(A color version of this figure is available in the online journal.)

In the last column, we quote the emission measure for each ion. This has been computed from the equation:

$$\mathrm{EM}_i = \frac{4\pi d^2 F_i}{\epsilon_i}, \tag{1}$$

where F_i is the measured line flux, ϵ_i is the line emissivity at T_{max}, and d is the distance to the star, which we take as $d = 301$ pc (Hipparcos; Perryman et al. 1997). As can be seen, values of EM_i are of the order of 10^{53-55} cm^{-3}. As stated before, the kT_{max} might not reflect the true temperature of the plasma and, therefore, the emissivity can have a lower value.

The S XVI 4.73 Å line presents a possible P Cygni profile (Figure 10). This possibility is rather interesting, since it would point to the stellar wind as one of the possible sites for X-ray
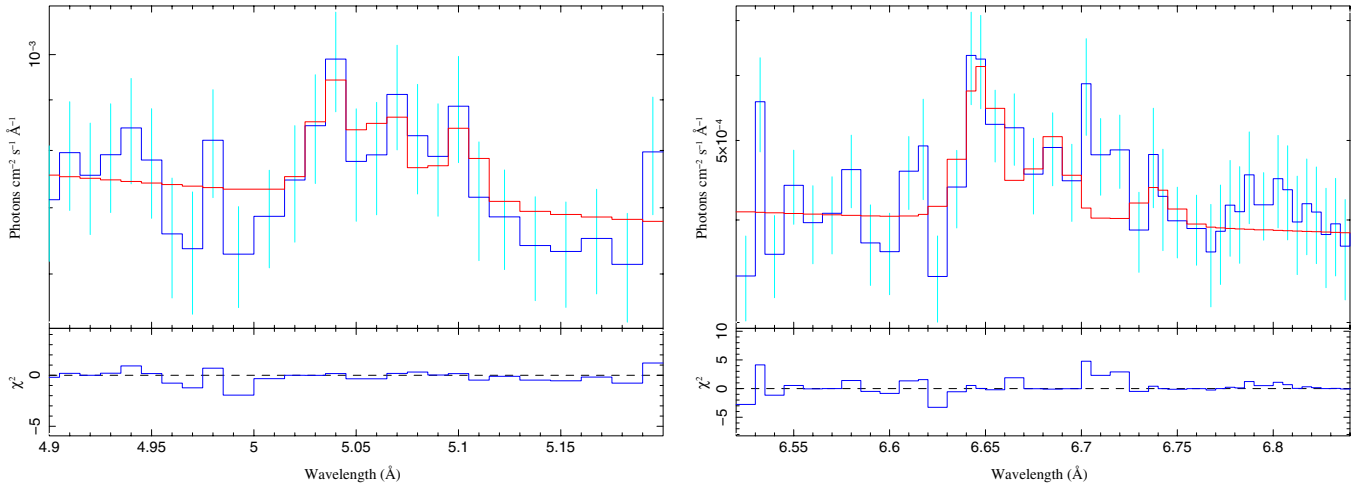
Figure 11. Top: S XV triplet. The *r*, *i*, and *f* components are clearly discerned. The positions and widths of the Gaussians have been fixed while the normalization is left free. Bottom: Si XIII triplet. The excess residuals at 6.72 Å are roughly consistent with Mg XII Lyγ because Mg XII Lyα is strong.
(A color version of this figure is available in the online journal.)

production in the system. P Cygni profiles have been observed by *Chandra* in the high-mass X-ray binaries Vela X-1 and Cyg X-3 (Vilhu et al. 2009). The blue absorption to red emission peak separation implies a velocity of $\sim$3400 km s^{-1}. Such high values have only been found in the terminal wind velocity v_∞ of very early type stars like the O3 star HD93129A (Taresch et al. 1997). This is, however, much larger than the wind velocity measured through the UV C IV lines (Smith & Balona 2006) in HD110432 and would rather suggest some violent localized outflow. Unfortunately, no other line presents such a profile in our spectrum and further monitoring will be required to address this issue.

4.3.1. He-like Triplets

Three He-like triplets have been identified in the spectrum. Although the S/N is low (see Figure 11), it can provide useful constraints, such as temperature and density diagnostics for the plasma (Porquet & Dubau 2000). The three lines visible in the triplets are called *r*, *i*, and *f*, which stand for the *resonance*, *intercombination*, and *forbidden* transitions, respectively. The models used in the previous section do not fit perfectly all the triplets *individually*. For example, the *bvapec* composite model is able to describe the *r* and *f* transitions of both S XV and Si XIII (although slightly underestimated) but does not show any detectable *i* transition. The *vmekal*, in turn, describes well the *r*, *i*, and *f* transitions in the Si XIII (albeit, again, underestimating all three lines) while they are undetectable in the S XV triplet. Therefore, we use the approach described previously where a Gaussian has been fitted to every transition (when present) over a multiple bremsstrahlung continuum.

Using values in Table 2 for the Si XIII triplet, we can compute the index $G = (i + f)/r = 0.73$, where *r*, *i*, and *f* stand for the fluxes of the corresponding lines in the triplet, respectively. This value is indicative of a high plasma temperature of the order of 10 MK. This is also supported by the presence of Mg XI, which is not too prominent if $T < 10^7$ K. On the other hand, the index $R = f/i = 0.42$ points to a high plasma density of the order of $n_e \approx 10^{13-14}$ cm^{-3}. The high density is also supported by the absence of the *f* component of the Mg XI triplet which tends to be suppressed at high densities. This value is consistent with the high end range deduced by Smith et al. (1998) for the hot plasma in γ Cas, namely, $n_e \approx 10^{13-14}$ cm^{-3}.

A strong UV radiation field can mimic a high density plasma because the *forbidden* line decreases due to the depopulation of the upper (^3S) levels via photoexcitation while the *intercombination* line is increased when the lower (^3P) levels are populated with these electrons (Porquet et al. 2001). Consequently, we have considered the possible influence of the intense UV radiation from the B0.5III star photosphere of blackbody temperature $T = 33,000$ K, diluted by a factor W. For that purpose, we shall use also the R value for the S XV triplet, $R = f/i = 0.86$. Blumenthal et al. (1972) have calculated the low density, low UV irradiation limit of this quantity, R_0, for Si XIII, 2.51, and for S XV, 2.04. The observed R value will depart from these values according to the equation

$$R = \frac{R_0}{1 + \frac{n_e}{n_c} + 2W\frac{\phi}{\phi_c}},$$

where ϕ is the photoexcitation rate and n_c and ϕ_c are the corresponding critical values for the plasma density and the photoexcitation rate, respectively, and W is the geometrical dilution factor. We see that $R \rightarrow R_0$ when $n_e \ll n_c$ (low density limit) and $\phi \ll \phi_c$ (low UV irradiation limit). Consequently, a value of R lower than (but not orders of magnitude lower than) R_0 means high densities and/or high UV irradiation of the X-ray emitting plasma. In order to gain some insight on the possible plasma emission location, we shall use the values of ϕ/ϕ_c tabulated by Blumenthal et al. (1972) for a blackbody of 10^5 K and dilution factor $W = 0.5$ (stellar surface), scaled here to the photospheric temperature $T = 33,000$ K and arbitrary W. We obtain $\phi/\phi_c = 74$ for Si XIII and $\phi/\phi_c = 17$ for S XV. We shall assume, further, an average plasma density for HD110432 of the order of $n_e \approx 10^{13}$ cm^{-3}, consistent with the observed R value for HD110432 and that derived for γ Cas. In that case, the $n_e/n_c \approx 1$ for Si XIII (for which $n_c = 4 \times 10^{13}$) while for S XV it will be $n_e/n_c \approx 0.1$ ($n_c = 1.9 \times 10^{14}$). With these values, we obtain dilution factors of 0.03 and 0.04 for Si XIII and S XV, respectively. Now, recalling that $W = (1/2)[1 - (1 - (R_*/r)^2)^{1/2}]$, where *r* is the distance from the X-ray plasma site to the stellar center, we can locate the plasma at a distance of $r \simeq (2-3)R_*$. Although the associated errors are large ($\sim$50%), the small values of R with respect to the low density, low UV flux limit make it clear that neither the density nor the irradiation terms can be neglected in the equation given

11

in Section 4.3.1, locating the emission sites relatively close to the photosphere of the Be star at $r < 3R_*$.

Alternatively, this intense UV radiation field could come from the radiation of a putative WD companion. For the sake of comparison, we will take the WD surface temperature of the order of 10^5 K. In such a case, this will be the primary ionizing field and we can use directly the values of ϕ/ϕ_c calculated by Blumenthal et al. (1972) to obtain dilution factors of $W = 0.76$ for Si XIII and $W = 0.2$ for S XV. These would translate into emission regions located at $r \sim [1.4–1.5]R_{\rm WD}$, respectively, in units of the (putative) WD radius. That is to say, the X-ray emission would be produced very close to the WD surface, as might be expected if the X-rays are produced via accretion.

4.3.2. The Fe Complex

In the first panel of Figures 7 and 8, we plot the *Chandra* HETG spectrum of the Fe complex modeled with three `vmekal` and `bvapec` components of different temperatures and absorption columns, respectively. Clearly, the highly ionized species are significantly broader than the line from neutral Fe. While the width of the latter is not resolved in the *Chandra* spectrum, the former show an FWHM ≈ 0.02 Å (see Table 2). Within the `vmekal` model, no additional correction has been applied. In the `bvapec` model, we modify the resulting spectrum with some turbulence velocity $v_{\rm turb}$. The hot component requires a $v_{\rm turb} \approx 1200 \, {\rm km \, s^{-1}}$, which can account perfectly for the broadening of these lines. Consequently, the warm and cool components do not require any turbulent broadening.

The Fe XXV line seems to present a double peak with $\Delta\lambda = 0.009$ Å. The circumstellar envelope in HD110432 is, contrary to the case of γ Cas, seen almost edge on. As a result, its optical spectrum clearly shows double-peaked Fe II emission lines (LO07). In the Fe XXV line, the $\Delta\lambda$ corresponds to a separation of $\sim 1500 \, {\rm km \, s^{-1}}$, which is much larger than the typical Keplerian velocity of the disk but of the order of the wind velocity.

The EW of the Fe Kα line is 89.78 eV. Using the curve of growth obtained by Torrejón et al. (2010), we get density columns of the reprocessing material $N_{\rm H} = 3 \times 10^{24}$ cm^{-2}. In contrast, the H density column obtained by Smith & Balona (2006) from optical spectra is $3^{+2}_{-1} \times 10^{22}$ cm^{-2}. Fluorescence emission is also seen from Si Kα, indicating the presence of large reservoirs of cold neutral material in the star or reflection off the (hypothetical) WD surface.

5. DISCUSSION

In general, we see that, despite its possible peculiarities (Lopes de Oliveira et al. 2010), the spectrum of HD110432 seems to be reminiscent of γ Cas (see, for example, Smith et al. 2004, Figure 2) strengthening the definition of the class. Consistent with LO07, the correct description of the spectrum requires at least three different thermal components of different temperatures and, as shown in this work, three different absorption columns. A hard tail is definitely present in HD110432 extending up to, at least, 50 keV. However, the nature of the hard component has not been unambiguously established for it can be equally well described by a thermal component or a power law. A power law could be a signature of synchrotron emission.

The absorption columns deduced from the fits to the X-ray continuum range from $N_{\rm H}^{\rm abs} \sim 0.15 \times 10^{22}$ cm^{-2} to 3×10^{22} cm^{-2}. The lower value is compatible with the ISM

medium (0.2×10^{22} cm^{-2}; Rachford et al. 2001). The high end value is consistent with the column deduced from the optical data for the envelope, namely, $N_{\rm H}^{\rm opt} = 3^{+2}_{-1} \times 10^{22}$ cm^{-2} (Smith & Balona 2006).

5.1. X-Ray Active Star or Accretion onto a WD?

The available data represent an isolated instance in the life of HD110432 and are insufficient, by itself, to settle this controversy. In principle, the described situation could be produced either by X-ray centers over the Be star photosphere in the active star disk interaction paradigm, or by accretion over a compact object orbiting relatively close to the stellar surface. Notwithstanding, we have presented here several pieces of evidence that can provide valuable new light onto the nature of the system when joined with previous results.

There is some evidence that the source is persistent. Indeed, it has been clearly detected by all the X-ray telescopes that have pointed at it: HEAO, *BeppoSAX*, *RXTE*, *XMM*, *Chandra*, and *Suzaku*. None of these observations were performed in any particular time or phase, yet the source was clearly detected and the light curve showed no eclipses. Unfortunately, those observations do not span in time enough to firmly conclude that the source is non-eclipsing. In order to check this hypothesis, we have analyzed the *RXTE*–All Sky Monitor (ASM) light curve for HD110432. The source is in the very limit of detection of ASM and most of the bins are compatible with zero flux. A continuum coverage with a large area collector ASM would be important to address this point. If we assume that the source is persistent and non-eclipsing, then either the X-ray emission is uniformly distributed over the area or the inclination of the system is such that the putative degenerate companion is never eclipsed.

As we have seen, the available data could favor an origin of the X-ray emission close to the stellar surface, at distances $r < 3R_*$ from the center of the Be star ($1R_*$ is the stellar surface). In such a case, the compact object should be placed in a orbit with radius $r < 3R_*$ with an orbital period between four and eight days. Given that we do not observe periodic outbursts at these periods, the orbit should be coplanar with the circumstellar disk. In order not to observe any eclipse, the inclination of the system should be such that $\cos i > R_*/r$, which delivers the constraint $i < 60°–70°$ for orbital radii of $2–3R_*$, respectively. This is very unlikely. The optical spectrum of HD110432 shows all its lines in emission with double peaks (see LO07, Figure 1; Smith & Balona 2006) clearly indicating that the system is seen with $i \approx 90°$.

On the other hand, as we have seen in the previous section, we cannot exclude that the X-ray emission is produced very close to the stellar surface $r \sim 1.5R_{\rm WD}$ of the putative WD companion. The multiplicity of absorbing columns is, however, difficult to reconcile with a single X-ray source embedded into the circumstellar disk. In any case, at least part of the X-ray emission appears to be absorbed by a column which is compatible with the density column of the circumstellar disk. Since the system is seen edge on, this would be in agreement with an X-ray source located close to the Be stellar surface which, in turn, argues in favor of the Be star photosphere being the main source of ionizing UV photons. The continuum monitoring of the source to detect or rule out the presence of eclipses would thus be important in understanding the nature of HD110432.

On the other hand, an X-ray emission distributed on or over the surface of the star could account naturally for the different absorbing density columns for each component as depicted in
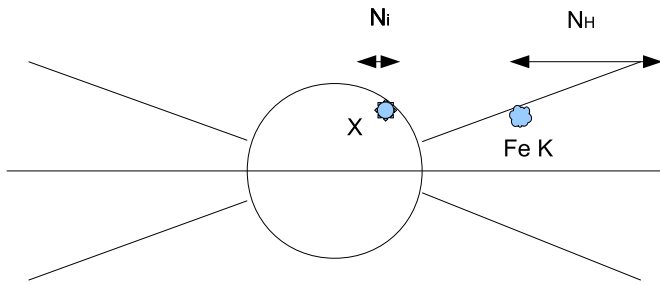
Figure 12. Sketch showing the possible location of an X-ray source, above the disk, based on Figure 4 of Smith et al. (2004). The source has an *emission* column N_i and illuminates the disk producing fluorescence. Both ion emission, Fe Kα, and continuum are absorbed by the same amount N_H from the circumstellar disk. The higher the latitude, the smaller the absorption. The observer is located to the right.

(A color version of this figure is available in the online journal.)

Figure 12. Since the system is seen close to edge on and the disk flares outward (in order to be in hydrostatic equilibrium), the lower the latitude of the X-ray source the higher the absorption. Thus, a number of small X-ray sources distributed on or above the stellar photosphere at several latitudes would account naturally for the characteristics of the observed emission.

The light curve shows a high variability and flaring but all efforts made so far have failed to detect any coherent pulsation. The persistent lack of detection of any coherent modulation strongly argues against the degenerate companion scenario. In conclusion, with the available data at hand, the X-ray active standalone star seems to emerge as the least problematic explanation. The mechanism behind such energetic emission, however, remains a mystery and is challenging. In particular, the extreme temperatures of the order of 15–30 keV or, alternatively, the presence of nonthermal components is not explained under this paradigm. The fact that other isolated Be stars with similar spectral types and comparably large circumstellar disks do not show any X-ray emission at all, is not explained either. Further observations will be required to establish the nature of this mysterious object. In particular, it would be necessary to (1) obtain a high S/N spectrum of the high energy tail in order to unambiguously establish the nature of the hard component using, for example, NuSTAR. This would require, probably, the *simultaneous* use of *Chandra* and/or *XMM-Newton*. (2) Monitor the star with an ASM to establish or rule out the persistence of the X-ray emission and the presence or lack of eclipses (with MAXI or LOFT), (3) and a monitoring campaign with a large collecting area telescope (to reduce the long exposure times) of the triplets to look for some periodic modulation that could arise from the (co)rotation of the X-ray center(s) around the star.

The authors acknowledge Myron Smith for his permission to use their original HETG γ Cas data in Figure 6. This

REFERENCES

Anders, E., & Grevesse, N. 1989, Geochim. Cosmochim. Acta, 53, 197
Balucinska-Church, McCammon 1992, ApJ, 400, 699
Blumenthal, G. R., Drake, G. W. F., & Tucker, W. H. 1972, ApJ, 172, 205
Canizares, C. R., Davis, J. E., Dewey, D., et al. 2005, PASP, 117, 1144
Donati, J., Babel, J., Howarth, I. D., & Semel, M. 2002, MNRAS, 333, 55
Donati, J., Howarth, I. D., Bouret, J.-C., et al. 2006a, MNRAS, 365, 6
Donati, J., Howarth, I. D., Jardine, M. M., et al. 2006b, MNRAS, 370, 629
Harmanec, P., Habuda, P., Štefl, S., et al. 2000, A&A, 364, L85
Houck, J. C., & Denicola, L. A. 2000, in ASP Conf. Ser 216, Astronomical Data Analysis Software and Systems IX, ed. N. Manset, C. Veillet, & D. Crabtree (San Francisco, CA: ASP), 591
Kaur, R., Wijnands, R., Patruno, A., et al. 2009, MNRAS, 394, 1597
Koyama, K., et al. 2007, PASJ, 59, 23
Kubo, S., Murakami, T., Ishida, M., & Corbet, R. H. D. 1998, PASJ, 50, 417
La Palombara, N., & Mereghetti, S. 2007, A&A, 474, L137
Lopes de Oliveira, R., & Motch, C. 2011, ApJ, 731, L6
Lopes de Oliveira, R., Motch, C., Haberl, F., Negueruela, I., & Janot-Pacheco, E. 2006, A&A, 454, 265
Lopes de Oliveira, R., Motch, C., Smith, M., Negueruela, I., & Torrejón, J. M. 2007, A&A, 474, 983, (LO07)
Lopes de Oliveira, R., Smith, M., & Motch, C. 2010, A&A, 512, A22
Martins, F., Donati, J., Marcolino, W. L. F., et al. 2010, MNRAS, 407, 1423
Mitsuda, K., Bautz, M., Inoue, H., et al. 2007, PASJ, 59, 1
Motch, C., Lopes de Oliveira, R., Negueruela, I., Haberl, F., & Janot-Pacheco, E. 2007, in ASP Conf. 361, Active OB-Stars: Laboratories for Stellar and Circumstellar Physics, ed. S. Stefl, S. P. Owocki, & A. T. Okazaki (San Francisco, CA: ASP), 117
Mukai, K., Kinkhabwala, A., Peterson, J. R., Kahn, S. M., & Paerels, F. 2003, ApJ, 586, L77
Okazaki, A. T., Bate, M. R., Ogilvie, G. I., & Pringle, J. E. 2002, MNRAS, 337, 967
Owens, A., Oosterbroek, T., Parmar, A. N., Stüwe, J. A., & Haberl, F. 1999, A&A, 348, 170
Perryman, M. A. C., Lindegren, L., Kovalevsky, J., et al. 1997, A&A, 323, 49
Porquet, D., & Dubau, J. 2000, A&AS, 143, 495
Porquet, D., Mewe, R., Dubau, J., Raasen, A. J., & Kaastra, J. S. 2001, A&A, 376, 1113
Rachford, B. L., Snow, T., Tumlinson, J., et al. 2001, ApJ, 555, 839
Raguzova, N. V. 2001, A&A, 367, 848
Rakowski, C. E., Schulz, N. S., Wolk, S. J., & Testa, P. 2006, ApJ, 649, L111
Robinson, R. D., Smith, M., & Henry, G. W. 2002, ApJ, 575, 435
Safi-Harb, S., Ribó, M., Butt, Y., et al. 2007, ApJ, 659, 407
Smith, M., & Balona, L. 2006, ApJ, 640, 491
Smith, M., Cohen, D. H., Feng Gu, M., et al. 2004, ApJ, 600, 972
Smith, M., Robinson, R. D., & Corbet, R. H. 1998, ApJ, 503, 877
Sturm, R., Haberl, F., Pietsch, W., et al. 2012, A&A, 537, 76
Takahashi, Abe, K., Endo, M., et al. 2007, PASJ, 59, 35
Taresch, G., Kudritzki, R. P., Hurwitz, M., et al. 1997, A&A, 321, 531
Torrejón, J. M., & Orr, A. 2001, A&A, 377, 148, (TO01)
Torrejón, J. M., Schulz, N. S., Nowak, M. A., & Kallman, T. 2010, ApJ, 715, 947
Vilhu, O., Hakala, P., Hannikainen, D. C., McCollough, M., & Koljonen, K. 2009, A&A, 501, 679
Waters, L. B. F. M., Pols, O. R., Hogeveen, J., et al. 1989, A&A, 220, L1